

Detecting intermediate-mass ratio inspirals from the ground and space

Pau Amaro-Seoane

*Institute of Space Sciences (ICE, CSIC) & Institut d'Estudis Espacials de Catalunya (IEEC) at Campus UAB,
Carrer de Can Magrans s/n 08193 Barcelona, Spain,
Institute of Applied Mathematics, Academy of Mathematics and Systems Science,
Chinese Academy of Sciences, Beijing 100190, China,
Kavli Institute for Astronomy and Astrophysics at Peking University, 100871 Beijing, China,
and Zentrum für Astronomie und Astrophysik, TU Berlin, Hardenbergstraße 36, 10623 Berlin, Germany*



(Received 10 July 2018; published 24 September 2018)

The detection of the gravitational capture of a stellar-mass compact object by a massive black hole (MBH) will allow us to test gravity in the strong regime. The repeated, accumulated bursts of gravitational radiation from these sources can be envisaged as a geodesic mapping of space-time around the MBH. These sources form via two-body relaxation, by exchanging energy and angular momentum, and inspiral in a slow, progressive way down to the final merger. The frequencies fall in the millihertz range for MBHs with masses $\sim 10^6 M_\odot$, i.e., that of space-borne gravitational-wave observatories such as LISA. In this article we show that, depending on their orbital parameters, intermediate-mass ratio inspirals (IMRIs) of MBHs with masses between a hundred and a few thousand M_\odot have frequencies that make them detectable (i) with ground-based observatories, or (ii) with both LISA and ground-based observatories (such as advanced LIGO/Virgo) and third-generation observatories [such as the Einstein Telescope (ET)]. The binaries have a signal-to-noise ratio large enough to ensure detection. More extreme values of the orbital parameters correspond to systems that are only detectable with ground-based detectors and in particular enter the LIGO/Virgo band in many different harmonics for masses up to $2000 M_\odot$. We show that environmental effects are negligible, so the source should not have this kind of complication. The accumulated phase shift is measurable with LISA and ET, and for some cases also with LIGO, so that it is possible to recover information about the eccentricity and formation scenario. For IMRIs with a total mass $\lesssim 2000 M_\odot$ and initial eccentricities up to 0.999, LISA can give an advanced warning to ground-based detectors with seconds of precision. The possibility of detecting IMRIs from the ground alone or combined with space-borne observatories opens new possibilities for gravitational-wave astronomy.

DOI: [10.1103/PhysRevD.98.063018](https://doi.org/10.1103/PhysRevD.98.063018)

I. INTRODUCTION

The typical size of a massive black hole (MBH), i.e., its Schwarzschild radius, is extremely tiny from the point of view of the host galaxy. For a $10^6 M_\odot$ MBH, this difference is roughly 10 orders of magnitude. However, we have discovered a deep link between the properties of the galaxy and those of the MBH, in particular between the mass of the MBH and the velocity dispersion σ of the spheroidal component of the galaxy [1]. Because the region of interest is difficult to resolve, the lower end of this correlation is uncertain. However, if we extend these correlations to smaller systems, globular clusters or ultracompact dwarf galaxies should harbor black holes with masses ranging between 10^2 and $10^4 M_\odot$, i.e., intermediate-mass black holes (IMBHs) (for a review, see Refs. [2,3]), although such black holes have never been robustly detected.

The best way to probe the nature of MBHs is with gravitational waves (GWs), which allow us to extract information that is unavailable electromagnetically.

Observing the gravitational capture and plunge of a compact object through the event horizon of a black hole is one of the main goals of the Laser Interferometer Space Antenna (LISA) mission [4]. A compact object of stellar mass—so dense that it overcomes the tidal forces of the MBH—is able to approach the central MBH very closely, emitting a large amount of gravitational radiation as orbital energy is radiated away. This causes the semimajor axis to shrink. This “doomed” object spends many orbits around the MBH before it is swallowed. The radiated energy, which can be thought of as a snapshot containing detailed information about the system, will allow us to probe strong-field gravitational physics. Depending on the mass ratio q , we consider either extreme-mass ratio inspirals, $q \gtrsim 10^4:1$ (EMRIs; see Refs. [5,6]), or intermediate-mass ratio inspirals, $q \sim 10^2\text{--}10^4:1$ (IMRIs; see e.g., Refs. [7–9]).

In galactic nuclei the predominant way of producing EMRIs is via two-body relaxation [5]. At formation, these sources have extremely large eccentricities, particularly if

the MBH is a Kerr black hole [10], which is what we should expect from nature. However, in globular clusters (which harbor MBHs in the IMBH range) the loss-cone theory—which is our tool to understand how EMRIs form (see, e.g., Refs. [11–13])—becomes very complex, mostly due to the fact that the IMBH is not fixed at the center of the system. It becomes even more difficult when we add the emission of GWs—another layer of complication for the Newtonian problem. As of now, we must rely on computer simulations to address this problem.

The joint detection of a GW source with different observatories has already been discussed in the literature, but not in the mass ratio range that is addressed in this work. The series of works [14–17] investigated the formation, evolution, inspiral, and merger of IMBH binaries with a mass ratio not larger than 10 and the prospects of multiband detection with LISA and LIGO/Virgo. The authors of Ref. [18] explored a joint detection by different GW detectors in more detail than the previous references in the context of bursting sources emitted by binaries in galactic nuclei, also with a mass ratio not larger than 10. After the first detections by LIGO, the prospect of detecting similar-mass-ratio stellar-mass black holes with masses of about $30 M_{\odot}$ with LIGO/Virgo and LISA was discussed in Ref. [19], and the authors of Ref. [20] clarified that this is only possible for eccentric binaries in that mass range.

In this paper we show that IMRIs, which typically form in globular clusters (but not excluding larger systems such as galactic nuclei and dense nuclear clusters), can be jointly detected by ground-based and space-borne observatories. In particular, Advanced LIGO and Virgo, and the proposed third-generation Einstein Telescope (ET) [21,22], will be able to detect IMRIs from very eccentric and hard binaries, which form via two-body relaxation or the parabolic capture of a compact object and abrupt loss of energy. This idea was first presented in Ref. [23], while the energy and angular momentum changes in the case of a hyperbolic orbit were previously presented in Ref. [24]; see also Refs. [25–29] for more recent works. However, LISA is deaf to these kinds of sources. For milder eccentricities and semimajor axes, however, the combined detection of IMRIs with LISA and LIGO/Virgo or ET is a real possibility. Due to the range of frequencies that these sources have, a decihertz observatory such as the DECi-hertz Interferometer Gravitational Wave Observatory [30], the Superconducting Omni-directional Gravitational Radiation Observatory [31,32], or the proposed geocentric TianQin Project [33] would enhance the prospects of detection.

For some systems, LISA can give advance warning to ground-based detectors weeks before the source appears in their bandwidth and with an accuracy of seconds (and possibly below) before the merger.

II. FORMATION OF INTERMEDIATE-MASS-RATIO INSPIRALS IN GLOBULAR CLUSTERS

In this work the sources of interest are inspirals of compact objects onto an IMBH with a mass ratio of about

$\sim 10^2\text{--}10^4 : 1$. The most accurate simulations of a globular cluster are the so-called direct-summation N -body algorithms. In this scheme, one directly integrates Newton's equations of motion between all stars in a cluster at every time step, with a regularization algorithm for binaries, so that any phenomenon associated with gravity naturally arises (see, e.g., Refs. [34–36], and the latter for the concept of regularization). Following the first implementation in Ref. [37], many modern direct-summation codes can mimic the effects of general relativity via a post-Newtonian expansion of the forces to be integrated (see Sec. IX of Ref. [38] for a review of stellar-dynamical relativistic integrators).

The first dynamical simulation that presented the formation and evolution of an IMRI down to a few Schwarzschild radii from coalescence using this scheme was presented in Ref. [39]. In one of the simulations we presented, we observed and tracked the spontaneous production of an IMRI between an IMBH of mass $M_{\text{BH}} = 500 M_{\odot}$ and a stellar-mass black hole of mass $m_{\text{CO}} = 26 M_{\odot}$. After a few Myrs the IMRI merges, and the IMBH receives a relativistic recoil [40–42] and escapes the whole cluster. It must be noted that the IMBH was in a binary with another compact object (a stellar-mass black hole) for almost the entire simulation. The IMBH exchanged companions a few times and was ionized for the last time very abruptly to form the last binary. This binary started with a very small semimajor axis of about $a \sim 10^{-5}$ pc and a very large eccentricity of $e = 0.999$, which fits within the parabolic capture mechanism of Ref. [23]. A few years later, the authors of Ref. [43] found similar results for a close range of masses but with a different approach. The work of Ref. [44] followed very closely the initial setup of Ref. [39] and reproduced our results with a different integrator, which corroborated our findings. Last, the numerical experiments of Ref. [45] explored IMBHs in a lighter range of masses around $M_{\text{BH}} = 150 M_{\odot}$. However, they also reported that the IMBH forms a binary about 90% of the time. The probability distribution of the semimajor axis peaks at about $\lesssim 10^{-5}$ pc.

III. LIGHT AND MEDIUM-SIZED IMRIs

The characteristic amplitude and the GW harmonics in the quadrupolar radiation approximation can be calculated following the scheme of Ref. [46], in which the orbital parameters change slowly due to the emission of radiation. This is emitted at every integer multiple of the orbital frequency, $\omega_n = n\sqrt{GM_{\text{BH}}/a^3}$, where a is the semimajor axis. The strain amplitude in the n th harmonic at a given distance D , normalized to the typical values of this work, is

$$h_n = g(n, e) \frac{G^2 M_{\text{BH}} m_{\text{CO}}}{D a c^4} \quad (1)$$

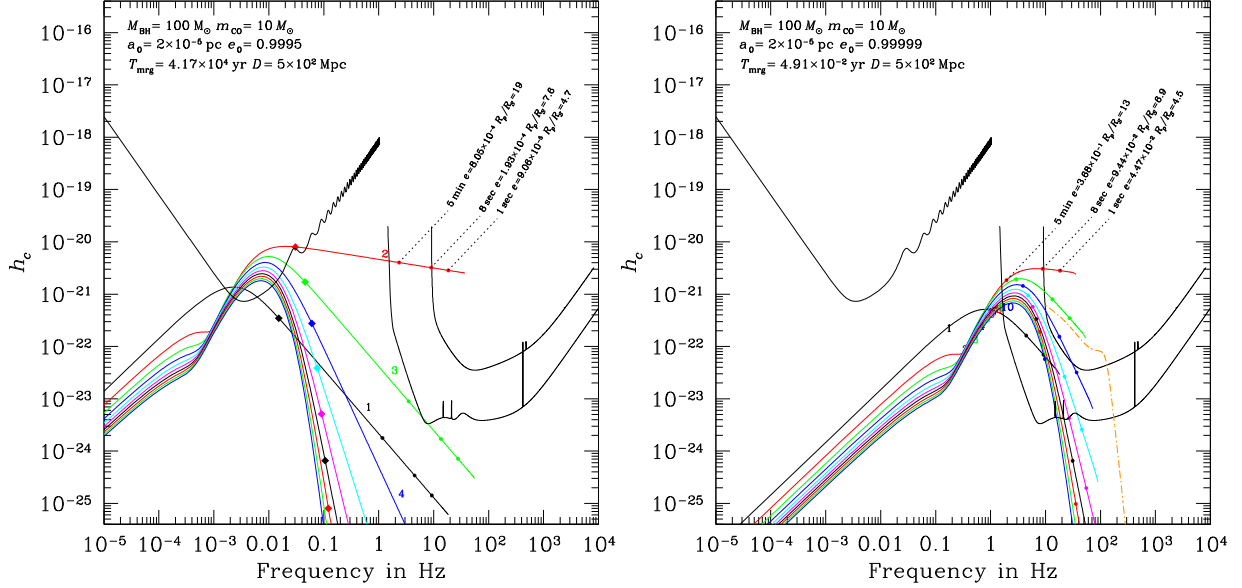


FIG. 1. Characteristic amplitude of the first ten harmonics emitted during the evolution of an IMRI. The solid V-shaped curve on the left corresponds to LISA’s intrinsic noise, and the two U-shaped curves on the right correspond to ET (lower h_c values) and Advanced LIGO. The mass of the IMBH is fixed to $M_{\text{MBH}} = 100 M_{\odot}$ and the mass of the compact object is $m_{\text{CO}} = 10 M_{\odot}$. The source is assumed to be located at a distance of $D = 500$ Mpc. Each panel corresponds to a binary with different initial values for the semimajor axis and eccentricity. The figure shows a few instants of time on the second harmonic in the evolution of the binary before the final merger. The total amount of time for the binary to merge from the initial values of the semimajor axis and eccentricity is given in each panel, T_{mrg} . The square symbol corresponds to 1 year before it. The rest of the harmonics also display the same instants of time using the same symbol but without a text label. The value of the eccentricity at that particular moment and the pericenter value R_p as a function of the Schwarzschild radius R_S are also shown. Additionally, the full waveform of the system in the LIGO sensitivity curve as approximated by the IMRPhenomD algorithm presented in Refs. [53,54] is depicted in the right panel by the dashed, orange curve.

$$\begin{aligned} &\simeq 8 \times 10^{-23} g(n, e) \left(\frac{D}{500 \text{ Mpc}} \right)^{-1} \left(\frac{a}{10^{-5} \text{ pc}} \right)^{-1} \\ &\times \left(\frac{M_{\text{BH}}}{10^3 M_{\odot}} \right) \left(\frac{m_{\text{CO}}}{10 M_{\odot}} \right). \end{aligned} \quad (2)$$

In this expression, M_{BH} is the mass of the IMBH, m_{CO} is the mass of the compact object (CO), and $g(n, e)$ is a function of the harmonic number n and the eccentricity e [see [46]]. We consider the rms amplitude averaged over the two GW polarizations and all directions. Other alternatives to this approach (such those in Refs. [47–50]) give a more accurate description of the last few orbits, but remain substantially equivalent to Ref. [46] at previous stages of the evolution. This approach correctly estimates the frequency cutoff at the innermost stable circular orbit frequency and is enough for the main goal of this work. (See also Ref. [51] for a discussion about the detection of binaries with mass ratios of 0.1 with advanced ground-based detectors using aligned-spin effective-one-body waveforms.)

With this approximation, we show in Fig. 1 h_c as a function of the frequency of two different IMRIs, and a few moments in the evolution before the final merger, which happens at a time T_{mrg} . For the kind of eccentricities that

we consider in this work, this time can be estimated following Ref. [52] for typical values as

$$\begin{aligned} T_{\text{mrg}} &\cong \frac{24\sqrt{2}(1-e_0)^{7/2}c^5}{85 G^3 M_{\text{BH}}^2 m_{\text{CO}}} a_0^4 \cong 6.4 \times 10^5 \text{ yrs} \quad (3) \\ &\times \left(\frac{M_{\text{BH}}}{10^3 M_{\odot}} \right)^2 \left(\frac{m_{\text{CO}}}{10 M_{\odot}} \right)^{-1} \left(\frac{R_p^0}{200 R_S} \right)^4 \\ &\times \left(\frac{1-e_0}{10^{-5}} \right)^{-1/2}, \end{aligned} \quad (4)$$

where R_p^0 and e_0 are the initial pericenter distance and eccentricity, respectively. In Fig. 1 the IMBH has a mass of $M_{\text{BH}} = 100 M_{\odot}$ and the mass of the CO is set to $10 M_{\odot}$. The figure shows the LISA sensitivity curve and those of Advanced LIGO (LIGO, henceforth) and ET in its D configuration [22], but the characteristic amplitude is shortened to start at lower values for clarity, since none of the sources considered achieve higher values. For reference, we also include the full waveform in the LIGO sensitivity curve as estimated by the IMRPhenomD approach of Refs. [53,54], which was developed to study systems with mass ratios of up to $q = 18$. This curve is close to the peak of harmonics in amplitude for this specific case, but in general this is not true and depends on the specifics of

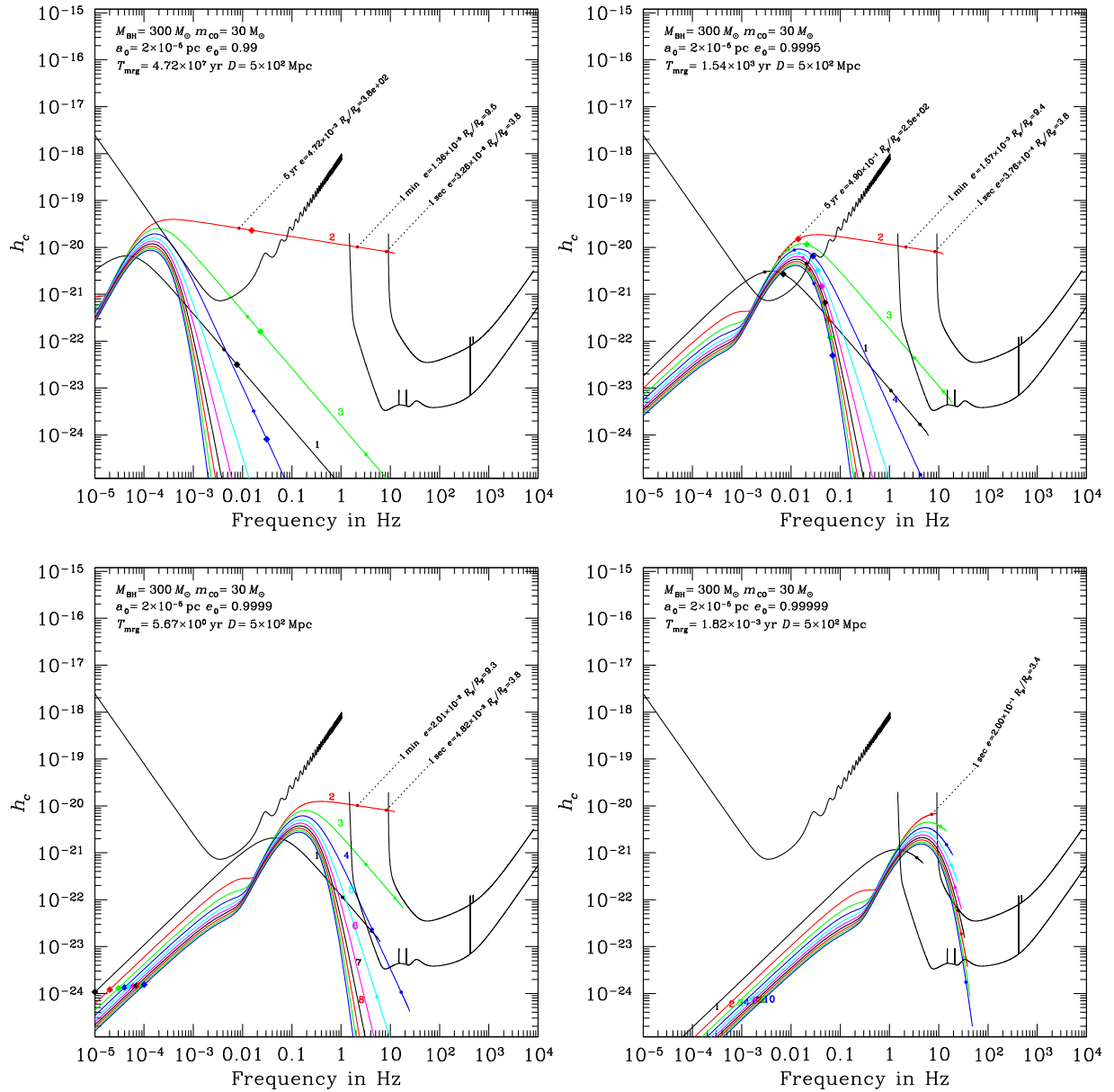


FIG. 2. Same as in Fig. 1 but for $M_{\text{MBH}} = 300 M_{\odot}$ and $m_{\text{CO}} = 30 M_{\odot}$ and with different labels in the evolution. Notice the displacement of the frequency peaks, which wander from the LISA band to the LIGO/Virgo one (top left panel to the bottom right one).

the binary, such as periastron argument, inclination angle, precession of the orbital plane, etc.

We can see that eccentricities corresponding to those that we can expect for a dynamical capture as described in the Introduction produce IMRIs which are observable with LISA and both ET and LIGO. In particular, the left panel corresponds to an IMRI that spends half a minute in LIGO. For lighter CO masses this time increases. For higher eccentricities (which can be achieved via two-body relaxation or in the parabolic braking scenario), at these masses the IMRIs can only be seen by ground-based detectors with a significant amount of detection time and with the vast majority of the harmonics in band. It is interesting to note

that ET may be able to detect up to several hundred events per year; see Refs. [55,56].

In Fig. 2 we show a more massive system, with a total mass of $310 M_{\odot}$. The source recedes in frequency due to the larger mass. For the systems considered in the upper panels, this allows IMRIs to spend more time in LISA and accumulate a larger signal-to-noise ratio (SNR), resulting in shortened time in the ground-based detectors which, however, is still significant. For the lower panels, however, LISA is again deaf to these sources.

Finally, in Fig. 3 we show a system similar to what was found in the numerical simulations of Ref. [39]. The mass

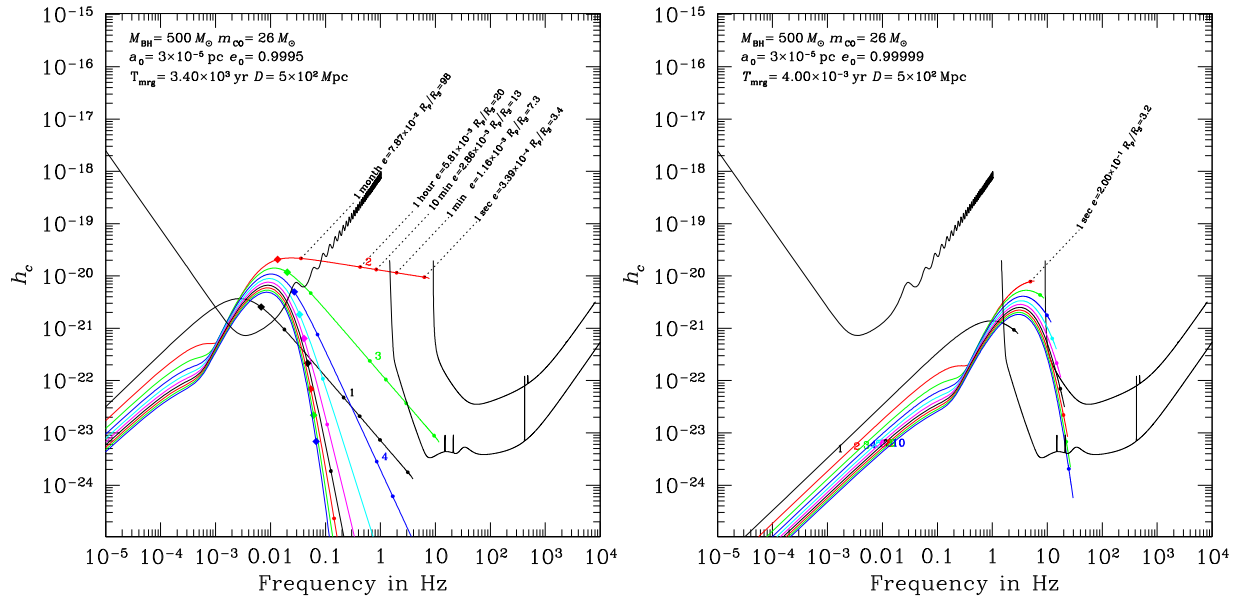


FIG. 3. Same as in Fig. 1 but for $M_{\text{MBH}} = 500 M_{\odot}$ and $m_{\text{CO}} = 26$, which is based on the relativistic stellar-dynamical simulation of Ref. [39]. The left panel corresponds to the kind of eccentricity in that work and the right one corresponds to a more extreme one, with different labels in the evolution.

of the IMBH is set to $500 M_{\odot}$. Higher-frequency sources are only observable by ground-based detectors.

IV. LARGE-MASS IMRIs

Figures 4–6 depict IMBHs with masses $M_{\text{BH}} = 1000 M_{\odot}$, $2000 M_{\odot}$, and $3000 M_{\odot}$, respectively. For more moderate eccentricities, the IMRIs in the examples can be detected with LISA and ET, but they do not enter the LIGO detection band. More extreme eccentricities lead to a large amount of harmonics entering the ET band for

significant amounts of time. In the case of a $2000 M_{\odot}$ IMBH, it can spend as much as 10 minutes in band in different harmonics. Larger masses (i.e., $3000 M_{\odot}$) produce short-lived sources that spend up to one minute in the ET detection band.

V. ENVIRONMENTAL EFFECTS

In the previous sections we have shown the evolution of an IMRI under the assumption that the binary is perfectly isolated from the rest of the stellar system, i.e., the binary

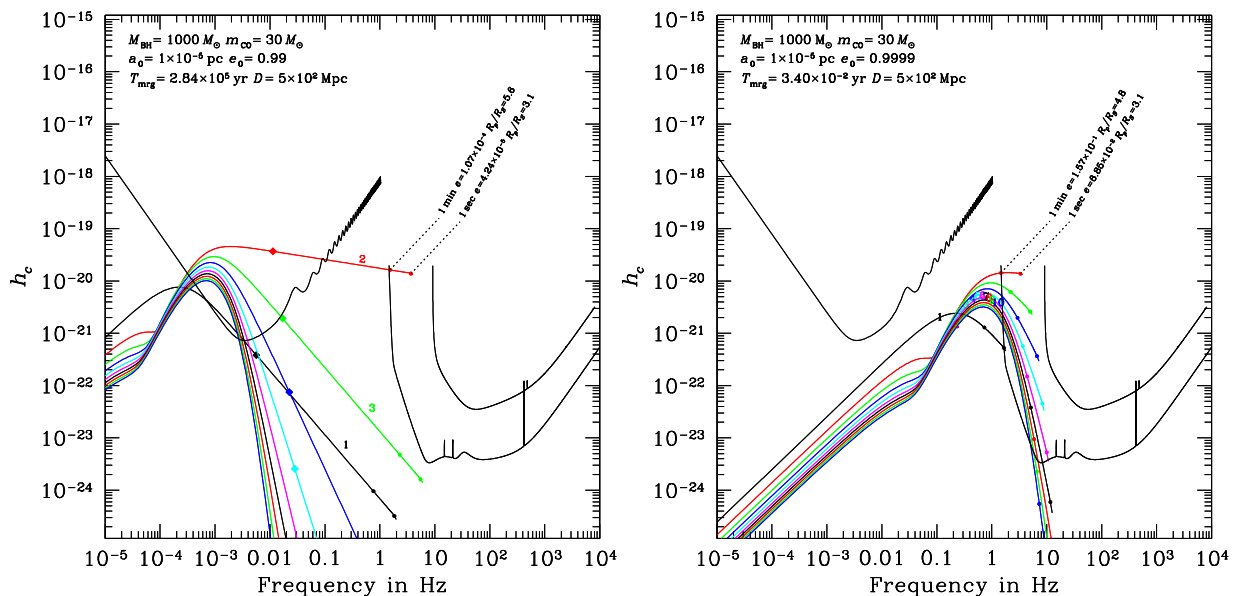


FIG. 4. Same as in Fig. 1 but for $M_{\text{MBH}} = 1000 M_{\odot}$ and $m_{\text{CO}} = 30$ and with different labels in the evolution.

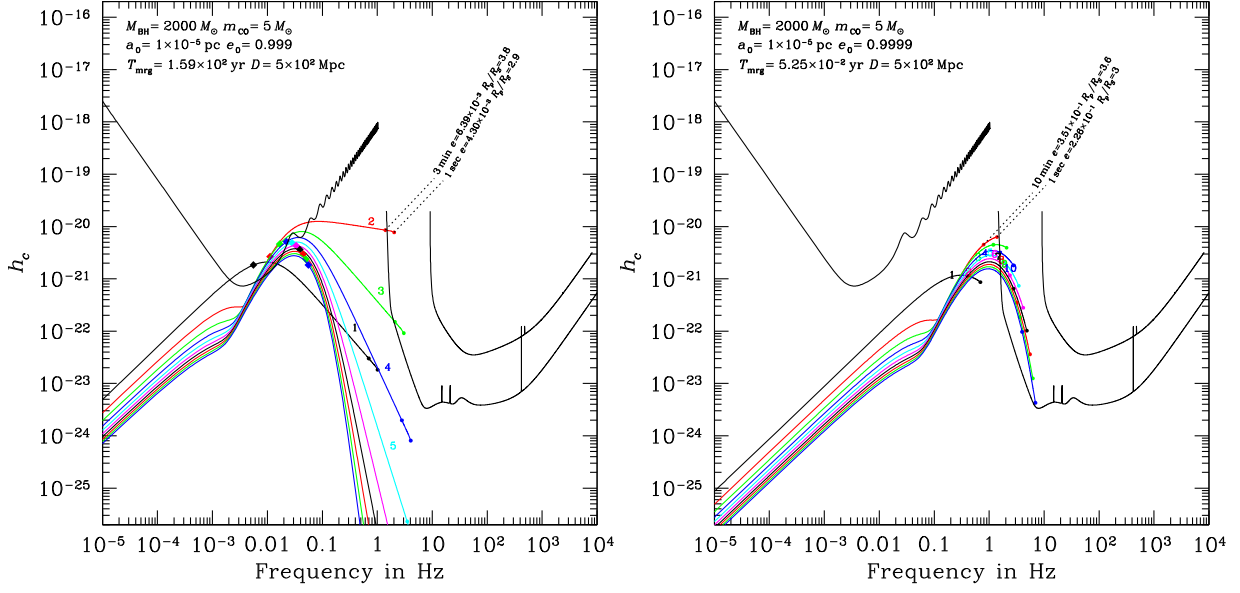


FIG. 5. Same as in Fig. 1 but for $M_{\text{MBH}} = 2000 M_{\odot}$ and $m_{\text{CO}} = 5$ and with different labels in the evolution.

evolves only due to the emission of GWs. The reason for this is that the problem is cleaner and easier to understand. However, the binary is located in a dense stellar system, (typically a globular cluster) and the role of gas is negligible, since the gas density in these systems is very low. Hence, to assess whether surrounding stars could vary or modify the evolution *after* the IMRI has formed, in this Sec. I investigate the impact of the stellar system using a semianalytical approach. The basic idea is to split the evolution of both the semimajor axis and the eccentricity

into two contributions: one driven by the dynamical interactions with stars (subscript D), and one due to the emission of GWs (subscript GW), $\dot{a} = \dot{a}_{\text{GR}} + \dot{a}_{\text{D}}$ and $\dot{e} = \dot{e}_{\text{GR}} + \dot{e}_{\text{D}}$, with dots representing a derivative with respect to time.

From Ref. [52],

$$\dot{a}_{\text{GW}} = -\frac{64 G^3 M_{\text{BH}} m_{\text{CO}} (M_{\text{BH}} + m_{\text{CO}})}{5 c^5 a^3 (1 - e^2)^{7/2}} \left(1 + \frac{73}{24} e^2 + \frac{37}{96} e^4 \right), \quad (5)$$

$$\dot{e}_{\text{GW}} = -\frac{304 G^3 M_{\text{BH}} m_{\text{CO}} (M_{\text{BH}} + m_{\text{CO}})}{15 c^5 a^4 (1 - e^2)^{5/2}} e \left(1 + \frac{121}{304} e^2 \right). \quad (6)$$

The GW terms are as given in Ref. [52]. Using the relationships of Ref. [57], we have that

$$\dot{a}_{\text{D}} = -H \frac{G\rho}{\sigma} a^2. \quad (7)$$

Following the usual notation, G is the gravitational constant, ρ is the stellar density around the binary, σ is the corresponding velocity dispersion of the cluster, and H is the so-called hardening constant, as introduced in Ref. [57]. For the kind of binaries we consider in this work (i.e., hard ones), we have that $(de/d\ln(1/a))_{\text{D}} = K(e)$. Since the density drops significantly during the evolution, we can regard σ as approximately constant and hence $de = K(e)d\ln(1/a) = -K(e)/ada$, so that $H \simeq 16$, as in the original work of Ref. [57] (see also Ref. [58]). Therefore,

$$\dot{e}_{\text{D}} = \frac{H}{\sigma} G\rho a K(e), \quad (8)$$

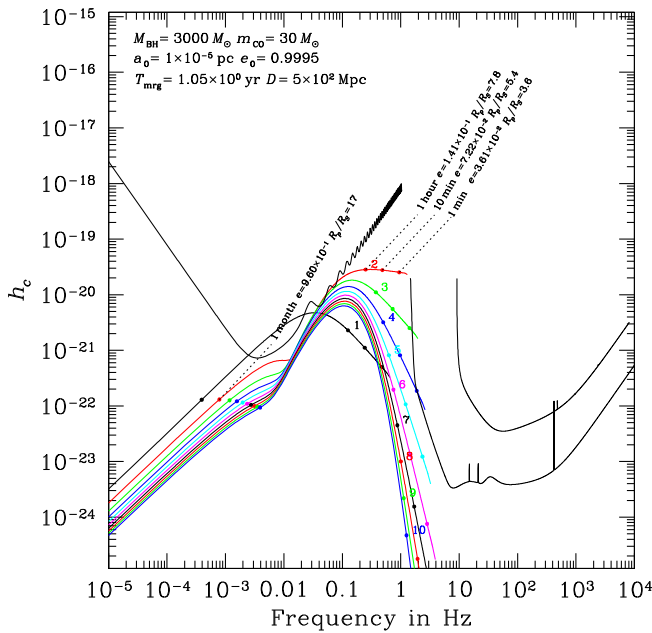


FIG. 6. Same as in Fig. 1 but for $M_{\text{MBH}} = 3000 M_{\odot}$ and $m_{\text{CO}} = 30$ and with different labels in the evolution.

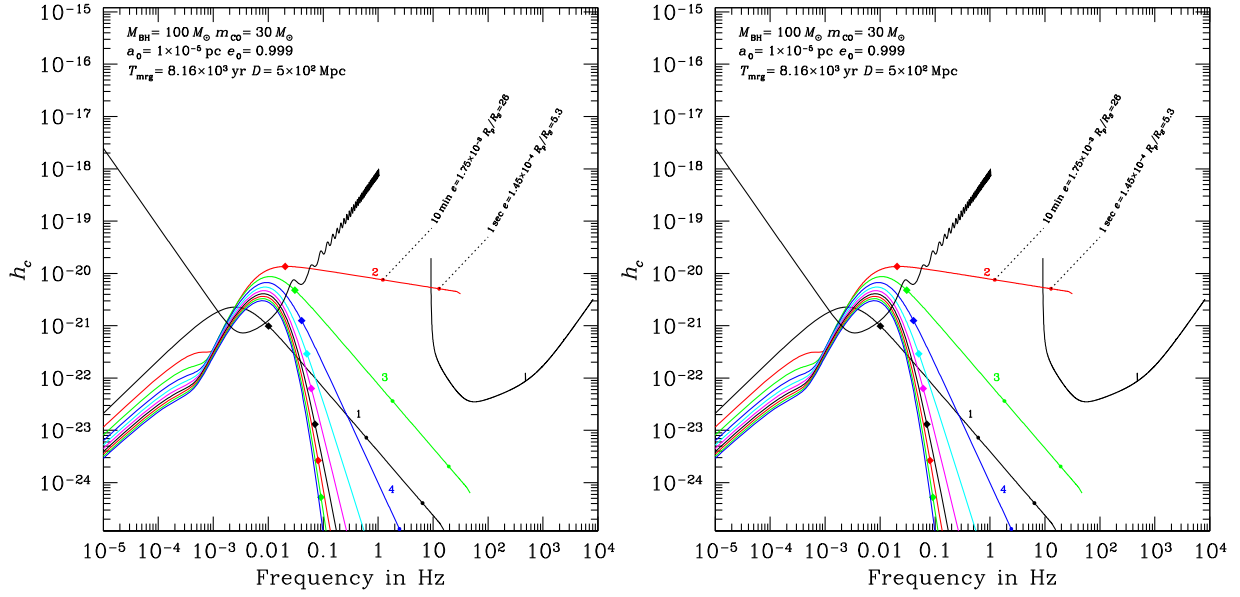


FIG. 7. (Left panel) As in Fig. 1 but for $M_{\text{MBH}} = 100 M_{\odot}$ and $m_{\text{CO}} = 30$ and with different labels in the evolution. (Right panel) Same as in the left panel but taking into account stellar dynamics (see text). We adopt an ambient stellar density of $2 \times 10^5 M_{\odot} \text{pc}^{-3}$, $K_0 = 0.1$, and a one-dimensional velocity dispersion of $\sigma = 15 \text{ km/s}$.

with $K(e) \sim K_0 e(1 - e^2)$, as in Ref. [59]. As an example, in Fig. 7 we show an IMRI formed by an IMBH of mass $M_{\text{BH}} = 100 M_{\odot}$ and a CO of mass $m_{\text{CO}} = 30 M_{\odot}$. The left panel corresponds to the case in vacuum, i.e., the binary evolves only due to the emission of GWs, and the right panel takes into account stellar dynamics. The reason for this choice of parameters is twofold: on the one hand, the impact of stellar dynamics on a lighter IMRI is more pronounced; on the other hand, K_0 has been estimated for more equal-mass binaries than the other cases. As expected, the effect of stellar dynamics on the binary at such a hardening stage is negligible, so the previous results hold even if we do not take into account the surrounding stellar system around the IMRI from the moment of formation. The previous dynamical story is however crucial for the initial orbital parameters of the binary.

VI. LOUDNESS OF THE SOURCES

A. Low-eccentricity sources: LIGO

As it inspirals, a compact binary becomes observable and more circular. The characteristic amplitude h_c of an IMRI emitting at a given frequency f is given by

$$h_c = \sqrt{(2\dot{E}/\dot{f})/(\pi D)}, \quad (9)$$

where \dot{E} is the power emitted, \dot{f} is the time derivative of the frequency, and D is the distance to the source [60]. The sky- and orientation-averaged SNR of a monochromatic source with the ansatz of ideal signal processing is given by the equation

$$\left(\frac{S}{N}\right)^2 = \frac{4}{\pi D^2} \int \frac{\dot{E}}{f S_h^{SA}(f) f^2} df \quad (10)$$

as derived in Ref. [60], where D is the distance to the source, \dot{E} is the rate of energy lost by the source, \dot{f} is the rate of change of frequency, and $S_h^{SA}(f) \approx 5S_h(f)$ is the sky- and orientation-averaged noise spectral density of the detector. For a source with multiple frequency components, the total SNR² is obtained by summing the above expression over each mode.

In Fig. 8 we show the Fourier-transformed waveform of both panels of Fig. 1, as approximated by the algorithm of Ref. [61]. There is a time-domain waveform that describes binary black holes evolving on mildly eccentric orbits, not exceeding $e \lesssim 0.2$. When the binaries enter the LIGO/Virgo band, even if they start with initially high eccentricities, they reach values below the threshold of the algorithm, which therefore is a good approximant to estimate the waveform and compute the SNR.

For the IMRI examples given in Fig. 1, assuming a distance of $D = 500 \text{ Mpc}$, we find SNRs in the LIGO bandwidth of 42.87 and 42.55 for the left and right panels, respectively. In Fig. 2, at the same distance, we find SNRs of 17.12, 17.13, 17.15, and 16.40 for the top-left, top-right, lower-left, and lower-right panels, respectively.

B. High-eccentricity sources

When moving to lower frequencies, the eccentricity greatly exceeds the limit of the approximation of Ref. [61] that we have used to derive the SNR. To calculate it when the IMRIs sweep the LISA bandwidth, we use the

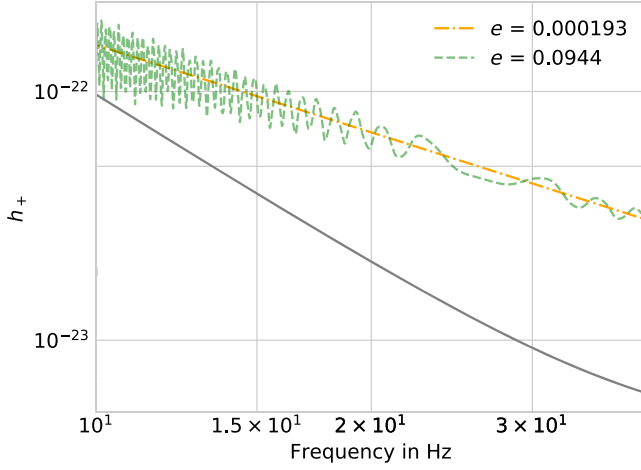


FIG. 8. Plus polarization h_+ for the two systems of Fig. 1 from the eccentricity of entrance into the LIGO bandwidth, i.e., when the frequency is of 10 Hz as approximated by the Fourier-transformed time-domain Taylor T4 algorithm of Ref. [61], which includes the effects of mild orbital eccentricity ($\lesssim 0.2$). The orange dot-dashed curve and the green dashed curve of higher eccentricity correspond to the left and right panels of Fig. 1, respectively. The solid grey curve shows the LIGO zero-detuned high-power design sensitivity.

expression (derived from Eq. 20 of Ref. [46], Eq. 2.1 of Ref. [60] and Eq. 56 of Ref. [49])

$$\left(\frac{S}{N}\right)_n^2 = \int_{f_n(t_{\text{ini}})}^{f_n(t_{\text{fin}})} \left(\frac{h_{c,n}(f_n)}{h_{\text{det}}(f_n)}\right)^2 \underbrace{\frac{1}{f_n} d(\ln(f_n))}_{\text{simply } df_n}. \quad (11)$$

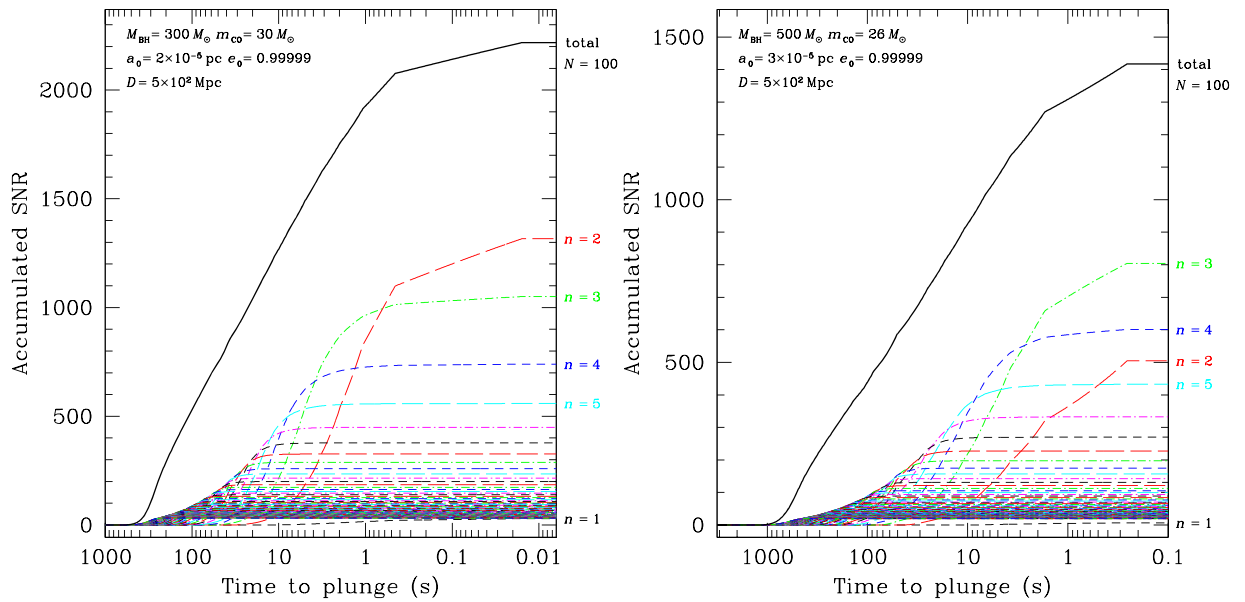


FIG. 9. (Left panel) Accumulated SNR in ET as a function of the time to plunge, T_{mrg} , in seconds, for the IMRI in the bottom-right panel of Fig. 2. we show the individual contributions of the first 100 harmonics and the total. (Right panel) Same for the right panel of Fig. 3.

In this equation, $f_n(t)$ is the (redshifted) frequency of the n th harmonic at time t ($f_n = n \times f_{\text{orbital}}$), $h_{c,n}(f_n)$ is the characteristic amplitude of the n th harmonic when the frequency associated to that component is f_n , and h_{det} is the square root of the sensitivity curve of the detectors.

Below we give a few examples of the SNRs for the IMRI systems in the LISA (ET) band of the previous sections, assuming a distance of 500 Mpc and taking the contribution of the first 100 harmonics.

- (1) Figure 1: Left panel: 15 (1036); right panel: 0.01 (1087).
- (2) Figure 2: Upper left panel: 50 (1994); upper right panel: 24 (1995); lower left panel: 2 (1991); lower right panel: 0.01 (2231).
- (3) Figure 3: Left panel: 36 (1449); right panel: 0.05 (1461).
- (4) Figure 4: Left panel: 79 (328); right panel: 0.4 (305).
- (5) Figure 5: Left panel: 7 (15); right panel: 0.1 (37).
- (6) Figure 6: 5 (1).

In Figs. 9 and 10 we give three examples of the accumulated SNR as calculated in this section. In the left and right panels of Fig. 9, we display the SNR in ET of the system in the bottom-right panel of Fig. 2 and the right panel of Fig. 3, respectively. In Fig. 10, we show the accumulated SNR of the system depicted in the left panel of Fig. 3 for LISA.

However, for LISA this is the total accumulated SNR for the total time that the source spends on band. The observational time (the time during which we retrieve data from the source) is in all cases shorter and, hence, the accumulated observed SNR is lower. As an example, for the left panel of Fig. 3, if we integrate all of the time the source spends on

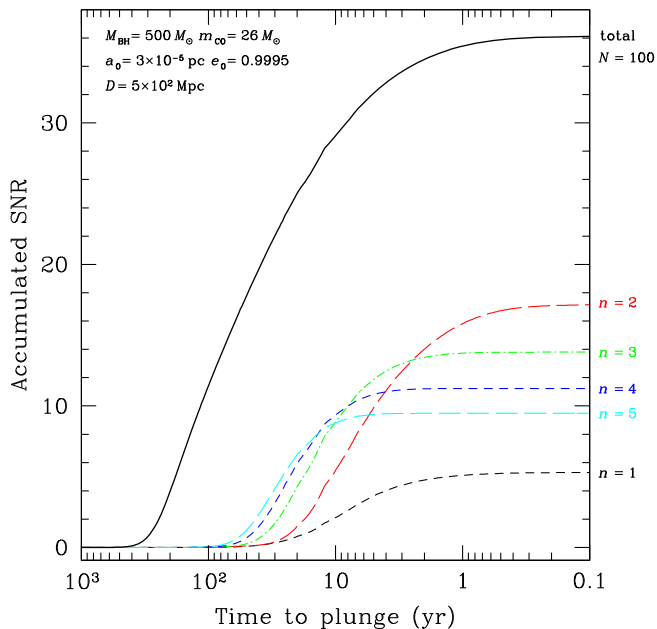


FIG. 10. Same as in Fig. 9 but for the same IMRI system in the left panel of Fig. 3, and in years. we show the individual contributions of the first ten harmonics, but the total SNR takes into account the contribution of the first 100, which are not displayed.

band we obtain the aforementioned SNR of 36. However, if we integrate the last 10 yrs before merger the SNR decreases to 23, and it decreases to 19 for the last 5 yrs. If we observed the source earlier in the evolution, say, e.g., 10 yrs before merger to 5 yrs before it, the SNR would be 14, and if we observed it 100 yrs before merger to 95 yrs before it, the SNR would be 3. As an example, Fig. 11 shows the accumulated

SNR for this system 10 and 5 yrs before the final plunge. This only applies to LISA, because the time spent in the ground-based detector ET is much shorter.

To assess whether this approach is robust, we now give the SNRs for the systems of Sec. VIA in the LIGO band, which have been calculated with the waveform model introduced in that section. In Fig. 1, as estimated with this approach, the SNRs for the left and right panels are 41 and 40, respectively. In Fig. 2, the SNRs from left to right and top to bottom are 12, 12, 11, and 14. These results are very close to those of Sec. VIA. The small differences arise from the fact that eccentricity tends to enhance the amount of energy emitted during the inspiral as the system radiates in band for longer. It is reasonable to take these estimates for circular orbits as a guideline for eccentric systems with masses similar to these. If the source is eccentric, since $a = R_{\text{per}}/(1 - e)$, a is larger at the time the source reaches a frequency of 10 Hz. The inspiral time depends on the value of a , and is larger for larger a . Another way to see this is that dE/dt is smaller when e is larger at fixed periastris (or frequency in our approximation). This is because at fixed periastris, increasing the eccentricity puts more of the orbit further from the MBH and hence the energy flux is on average reduced. As dE/dt is smaller, it takes longer to inspiral. This also explains why the SNR is slightly lower: dE/dt is lower at fixed periastris and thus at fixed frequency in this approximate model (physically, energy is being radiated out of band so we do not detect all of it).

VII. ACCUMULATED PHASE SHIFT

Understanding how IMRIs form and the values of their orbital parameters can help us to reverse engineer the

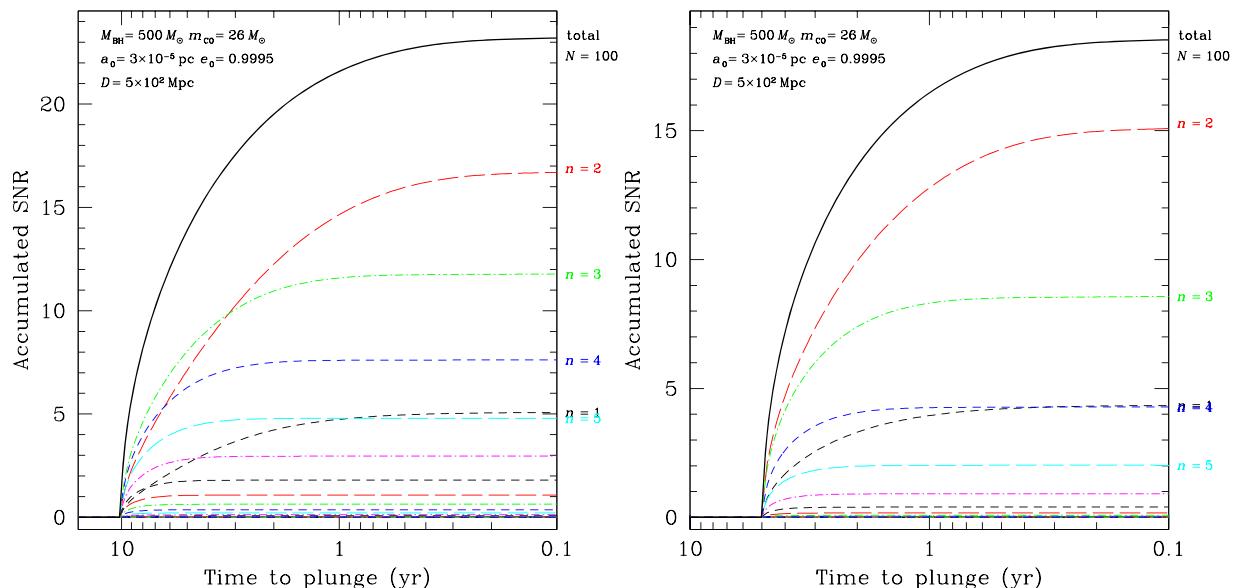


FIG. 11. Same as in Fig. 10 but taking into account only the SNR accumulated 10 (left panel) and 5 (right panel) years before the merger. See discussion in text.

environmental properties of the host cluster. Although the IMRIs considered in this work have very large initial eccentricities, when they reach the LIGO/Virgo band the eccentricity is virtually zero. It is however important to measure a nonzero eccentricity, because it can be a constraint on the formation mechanism as well as the stellar environment of the IMRI. If a residual eccentricity is present, it will induce a difference in the phase evolution of the signal as compared to a circular inspiral. Thanks to the derivation in Ref. [62] of the phase correction due to nonzero eccentricities, we can estimate the accumulated phase shift to lowest post-Newtonian order and to first order in e^2 with

$$\begin{aligned}\Delta\Psi_e(f) &= \Psi_{\text{last}} - \Psi_i \cong -\Psi_i \\ &= \frac{7065}{187136} e_i^2 (\pi f M_z)^{-5/3}.\end{aligned}\quad (12)$$

In the last equation, e_i is the eccentricity at the frequency of the dominant harmonic at which it enters the detector bandwidth, f is the frequency for the $n = 2$ harmonic, and we have introduced the quantity $M_z := (1+z)G(M_{\text{BH}} \times m_{\text{CO}})^{3/5} (M_{\text{BH}} + m_{\text{CO}})^{-1/5} / c^3$. Also, we made the approximation that $\Delta\Psi_e(f) = \Psi_{\text{last}} - \Psi_i \cong -\Psi_i$, where Ψ_{last} and Ψ_i are the final and initial phase, because of the pronounced fall-off of $\Psi_e(f)$ with increasing frequency; see the discussion in Sec. B.2 of Ref. [63].

To derive the accumulated phase shift in terms of f and the remaining time to merger, we now recall from Ref. [64] that the semimajor axis of the binary is

$$a^3 = \frac{G(M_{\text{BH}} + m_{\text{CO}})}{(\pi f)^2}.\quad (13)$$

The time for merger for $e \ll 1$ can be derived from Ref. [52] as follows:

$$\begin{aligned}T_{\text{mrg}} &\cong \frac{5}{256} \frac{c^5}{G^3 M_{\text{BH}} \times m_{\text{CO}} (M_{\text{BH}} + m_{\text{CO}})} \\ &\times \left[\frac{G(M_{\text{BH}} + m_{\text{CO}})}{(\pi f)^2} \right]^{4/3}.\end{aligned}\quad (14)$$

Last, let us recall that

$$e^2 f^{19/9} \cong \text{constant},\quad (15)$$

which can be derived from Eq. 5.12 of Ref. [52] with $1/(1 - e^2) \simeq 1$ combined with Eq. (13),¹ i.e., $a \propto f^{-2/3}$.

¹As described in *Astronomia nova*, ‘‘Sed res est certissima exactissimaque quod proportiō qua est inter binōrum quōrumcunque Planetārum tempora periodica, sit praecise sesquialtera proportionis mediārum distantiarum (...)’’.

Therefore, if we use Eq. (13) in Eq. (14), we obtain

$$\pi f \cong \left(\frac{5}{256} \right)^{3/8} M_z^{-5/8} T_{\text{mrg}}^{-3/8}.\quad (16)$$

Hence, using Eqs. (12), (15), and (16), we have that the accumulated phase shift in terms of f , $e_i(f)$, M_z , and T_{mrg} is

$$\begin{aligned}\Delta\Psi_e(f) &= \left(\frac{5}{256} \right)^{-17/12} \frac{7065}{187136} (\pi f_i)^{19/9} e_i^2 M_z^{25/36} T_{\text{mrg}}^{17/12} \\ &\cong 10 (\pi f_i)^{19/9} e_i^2 M_z^{25/36} T_{\text{mrg}}^{17/12}.\end{aligned}\quad (17)$$

The accumulated phase shift is detectable if $\gtrsim \pi$. With this approximation, we find the following phase shifts (in radians) for the IMRI systems presented in the previous sections, imposing a minimum threshold SNR of 5 (the numbers correspond to the panels of the figures from top to bottom and left to right):

- (i) LISA, taking into account only the last 5 years before merger: Fig. 1 has a negligible phase shift; Fig. 2: $180, 3.4 \times 10^6$, and the other two panels have a negligible phase shift; Fig. 3: 1.5×10^6 and the right panel is negligible; Fig. 4: 8200 and the right panel is negligible; Fig. 5: 9.7×10^5 and the right panel is negligible; Fig. 6 also has a negligible phase shift.
- (ii) ET: Figure 1: $\sim 5.1 \times 10^{-3}$ and 19 000; Fig. 2: $\sim 2.6 \times 10^{-7}$, $\sim 3.4 \times 10^{-3}$, 0.66, and 4600; Fig. 3: 1.3×10^{-3} and 3900; Fig. 4: 3.5×10^{-6} and 450; Fig. 5: 1.3×10^{-2} and 2600. Figure 6 has a negligible phase shift.
- (iii) LIGO: Figure 1: 4×10^{-6} and 1.2; Fig. 2: 1.1×10^{-10} , 1.4×10^{-6} , 2.3×10^{-4} , and 10. The rest of the cases have negligible phase shifts.

VIII. CONCLUSIONS

Intermediate-mass-ratio inspirals are typically formed in dense stellar systems such as galactic nuclei and globular clusters, typically with very large eccentricities (from $e=0.999$) and small semimajor axes (below $a \sim 10^{-5}$ pc), as found in a number of stellar-dynamics simulations of globular clusters [29,39,43–45]. Besides classical two-body relaxation, an interesting way of explaining the formation of these sources is the parabolic capture mechanism described in Refs. [23,25].

In this work we showed that IMRIs in clusters are not only detectable by space-borne observatories such as LISA; depending on the properties of the IMRIs, they can also be detected in conjunction with LIGO/Virgo or ET, and thus ground-based and space-borne observatories should be envisaged as one instrument if they are operated simultaneously.

I have considered IMBHs with masses ranging between $M_{\text{BH}} = 100 M_{\odot}$ and $3000 M_{\odot}$ and COs with different masses. We have separated them into light and medium-sized IMRIs for IMBHs with masses up to $500 M_{\odot}$ (which is a particular case based on the findings of Ref. [39]) and large-mass IMRIs for masses between $1000 M_{\odot}$ and $3000 M_{\odot}$.

I found that light and medium-sized IMRIs can be observed by LISA and ground-based detectors for eccentricities from 0.99 to 0.9995. In the range of frequencies detectable by LIGO/Virgo, they spend a maximum of about one minute on band. Higher-eccentricity sources, however, can only be detected by ground-based detectors (see Ref. [20] for a discussion on the role of eccentricity for low-mass-ratio binaries). This is due to the fact that as the eccentricity increases the pericenter distance decreases, so that the characteristic frequency of the GWs emitted at the pericenter increases (see Eq. 37 of Ref. [65] for a derivation of the peak frequency in the same approximation used in this work). In some cases, the full cascade of harmonics falls entirely within the bandwidth of the ground-based detectors.

The peak of large-mass IMRIs recedes in frequency compared to light and medium-sized ones, so that the cascade of harmonics is shifted towards the LISA domain. However, for eccentricities below 0.9995, IMRIs with IMBHs covering the full range of masses considered in this work ($100 M_{\odot}$ to $3000 M_{\odot}$) should be detectable with LISA with modest to large SNRs (from a few to tens) depending on the eccentricity and duration of the observation. For ground-based detectors, we computed the SNR for LIGO using the waveforms from a Fourier transformation of the time-domain Taylor T4 algorithm of Ref. [61] (limited to eccentricities $\lesssim 0.2$) and derived large enough SNRs (always of about a few 10).

Lower-frequency sources require larger eccentricities, and we cannot use these waveforms. For these detectors we used an approximate scheme to calculate the SNR, and we compared it with the previous results for LIGO and found that the approach is robust. The values for the SNR with ET can reach as much as ~ 2000 , and are of typically a few hundred and of tens for masses up to $2000 M_{\odot}$. LISA has SNRs of order 10, which significantly decrease when the harmonics peak of the IMRI system is closer to the ground-based regime.

By combining ground-based and space-borne observations we can impose better constraints on a system's parameters. On the one hand, LISA can observe the inspiral and hence provide us with measurements of parameters

such as the chirp mass. On the other hand, ground-based detectors detect the merger and ringdown, and therefore measure other parameters such as the final mass and spin. Thanks to this joint detection, one can split various degeneracies and get better measurements of the parameters, as compared to individual detections.²

Using a semianalytical approach, we have estimated the possible influence of the environment *after* their formation and found no impact, which will make it easier to detect and interpret IMRIs, because they are clean sources.

By looking at the accumulated phase shift, one could investigate the origin of light IMRIs thanks to a residual eccentricity. We found that LISA binaries typically accumulate hundreds of thousands and up to millions of radians, while ET binaries can accumulate up to 19 000 radians (typically a few thousand). While IMRI binaries are present within LIGO for a much shorter time, there is a case which does accumulate enough radians.

LISA can warn ground-based detectors at least one year in advance and with seconds of precision, and thus this observatory along with LIGO/Virgo and ET should be thought of as a single detector if they operate at the same time. Until LISA is launched, the perspective of detecting IMRIs from the ground opens new possibilities.

ACKNOWLEDGMENTS

I acknowledge support from the Ramón y Cajal Programme of the Ministry of Economy, Industry and Competitiveness of Spain, as well as the COST Action GWverse CA16104. I thank Marc Freitag for his help in the implementation of the SNR equations in the plotting subroutines, and for extended discussions about the phase shift. I am indebted with Leor Barack, Chen Xian, Bernard Schutz, Thomas Dent, and Matthew Benacquista for general comments, with Frank Ohme for his help with the waveforms, and with Jon Gair for discussions about SNR. This work started during a visit to La Sapienza university. I thank Roberto Capuzzo Dolcetta, Raffaella Schneider, Piero Rapagnani, Luigi Stella, Valeria Ferrari, Paolo Pani and Leonardo Gualtieri for their extraordinary hospitality. In particular I thank the students who took part in my course, because the many discussions and homework preparation led me to think about this problem.

²Christopher Berry, personal communication.

[1] J. Kormendy and L. C. Ho, *Annu. Rev. Astron. Astrophys.* **51**, 511 (2013).
[2] M. Mezcua, *Int. J. Mod. Phys. D* **26**, 1730021 (2017).

[3] N. Lützgendorf, M. Kissler-Patig, N. Neumayer, H. Baumgardt, E. Noyola, P. T. de Zeeuw, K. Gebhardt, B. Jalali, and A. Feldmeier, *Astron. Astrophys.* **555**, A26 (2013).

- [4] P. Amaro-Seoane *et al.*, [arXiv:1702.00786](#).
- [5] P. Amaro-Seoane, *Living Rev. Relativity* **21**, 4 (2018).
- [6] P. Amaro-Seoane, J. R. Gair, A. Pound, S. A. Hughes, and C. F. Sopuerta, *J. Phys. Conf. Ser.* **610**, 012002 (2015).
- [7] P. Amaro-Seoane, J. R. Gair, M. Freitag, M. C. Miller, I. Mandel, C. J. Cutler, and S. Babak, *Classical Quantum Gravity* **24**, R113 (2007).
- [8] D. A. Brown, J. Brink, H. Fang, J. R. Gair, C. Li, G. Lovelace, I. Mandel, and K. S. Thorne, *Phys. Rev. Lett.* **99**, 201102 (2007).
- [9] C. L. Rodriguez, I. Mandel, and J. R. Gair, *Phys. Rev. D* **85**, 062002 (2012).
- [10] P. Amaro-Seoane, C. F. Sopuerta, and M. D. Freitag, *Mon. Not. R. Astron. Soc.* **429**, 3155 (2013).
- [11] J. Binney and S. Tremaine, *Galactic Dynamics*, 2nd ed. (Princeton University, Princeton, NJ, 2008).
- [12] D. Heggie and P. Hut, *The Gravitational Million-Body Problem: A Multidisciplinary Approach to Star Cluster Dynamics* (Cambridge University Press, Cambridge, England, 2003).
- [13] L. Spitzer, *Dynamical Evolution of Globular Clusters* (Princeton University, Princeton, NJ, 1987).
- [14] P. Amaro-Seoane and M. Freitag, *Astrophys. J. Lett.* **653**, L53 (2006).
- [15] P. Amaro-Seoane, M. C. Miller, and M. Freitag, *Astrophys. J. Lett.* **692**, L50 (2009).
- [16] P. Amaro-Seoane, C. Eichhorn, E. K. Porter, and R. Spurzem, *Mon. Not. R. Astron. Soc.* **401**, 2268 (2010).
- [17] P. Amaro-Seoane and L. Santamaría, *Astrophys. J.* **722**, 1197 (2010).
- [18] B. Kocsis and J. Levin, *Phys. Rev. D* **85**, 123005 (2012).
- [19] A. Sesana, *Phys. Rev. Lett.* **116**, 231102 (2016).
- [20] X. Chen and P. Amaro-Seoane, *Astrophys. J. Lett.* **842**, L2 (2017).
- [21] B. Sathyaprakash *et al.*, *Classical Quantum Gravity* **29**, 124013 (2012).
- [22] S. Hild *et al.*, *Classical Quantum Gravity* **28**, 094013 (2011).
- [23] G. D. Quinlan and S. L. Shapiro, *Astrophys. J.* **343**, 725 (1989).
- [24] R. O. Hansen, *Phys. Rev. D* **5**, 1021 (1972).
- [25] B. Kocsis, M. E. Gáspár, and S. Márka, *Astrophys. J.* **648**, 411 (2006).
- [26] I. Mandel, D. A. Brown, J. R. Gair, and M. C. Miller, *Astrophys. J.* **681**, 1431 (2008).
- [27] R. O’Leary, B. Kocsis, and A. Loeb, *Mon. Not. R. Astron. Soc.* **395**, 2127 (2009).
- [28] W. H. Lee, E. Ramirez-Ruiz, and G. van de Ven, *Astrophys. J.* **720**, 953 (2010).
- [29] J. Hong and H. M. Lee, *Mon. Not. R. Astron. Soc.* **448**, 754 (2015).
- [30] S. Kawamura *et al.*, *Classical Quantum Gravity* **28**, 094011 (2011).
- [31] H. J. Paik, C. E. Griggs, M. Vol Moody, K. Venkateswara, H. M. Lee, A. B. Nielsen, E. Majorana, and J. Harms, *Classical Quantum Gravity* **33**, 075003 (2016).
- [32] J. Harms and H. J. Paik, *Phys. Rev. D* **92**, 022001 (2015).
- [33] J. Luo, L.-S. Chen, H.-Z. Duan, Y.-G. Gong, S. Hu, J. Ji, Q. Liu, J. Mei, V. Milyukov, M. Sazhin, C.-G. Shao, V. T. Toth, H.-B. Tu, Y. Wang, Y. Wang, H.-C. Yeh, M.-S. Zhan, Y. Zhang, V. Zharov, and Z.-B. Zhou, *Classical Quantum Gravity* **33**, 035010 (2016).
- [34] S. J. Aarseth, *Publ. Astron. Soc. Pac.* **111**, 1333 (1999).
- [35] S. J. Aarseth, *Gravitational N-Body Simulations* (Cambridge University Press, Cambridge, England, 2003).
- [36] S. J. Aarseth and K. Zare, *Celest. Mech.* **10**, 185 (1974).
- [37] G. Kupa, P. Amaro-Seoane, and R. Spurzem, *Mon. Not. R. Astron. Soc. Lett.* **371**, L45 (2006).
- [38] P. Amaro-Seoane, *Living Rev. Relativity* **21**, 4 (2018).
- [39] S. Konstantinidis, P. Amaro-Seoane, and K. D. Kokkotas, *Astron. Astrophys.* **557**, A135 (2013).
- [40] M. Campanelli, C. O. Lousto, P. Marronetti, and Y. Zlochower, *Phys. Rev. Lett.* **96**, 111101 (2006).
- [41] J. G. Baker, J. Centrella, D.-I. Choi, M. Koppitz, J. R. van Meter, and M. C. Miller, *Astrophys. J. Lett.* **653**, L93 (2006).
- [42] J. A. González, U. Sperhake, B. Brügmann, M. Hannam, and S. Husa, *Phys. Rev. Lett.* **98**, 091101 (2007).
- [43] N. W. C. Leigh, N. Lützendorf, A. M. Geller, T. J. Maccarone, C. Heinke, and A. Sesana, *Mon. Not. R. Astron. Soc.* **444**, 29 (2014).
- [44] C.-J. Haster, F. Antonini, V. Kalogera, and I. Mandel, *Astrophys. J.* **832**, 192 (2016).
- [45] M. MacLeod, M. Trenti, and E. Ramirez-Ruiz, *Astrophys. J.* **819**, 70 (2016).
- [46] P. C. Peters and J. Mathews, *Phys. Rev.* **131**, 435 (1963).
- [47] V. Pierro, I. M. Pinto, A. D. Spallicci, E. Laserra, and F. Recano, *Mon. Not. R. Astron. Soc.* **325**, 358 (2001).
- [48] K. Glampedakis, S. A. Hughes, and D. Kennefick, *Phys. Rev. D* **66**, 064005 (2002).
- [49] L. Barack and C. Cutler, *Phys. Rev. D* **69**, 082005 (2004).
- [50] J. R. Gair and K. Glampedakis, *Phys. Rev. D* **73**, 064037 (2006).
- [51] J. Veitch, M. Pürrer, and I. Mandel, *Phys. Rev. Lett.* **115**, 141101 (2015).
- [52] P. C. Peters, *Phys. Rev.* **136**, B1224 (1964).
- [53] S. Husa, S. Khan, M. Hannam, M. Pürrer, F. Ohme, X. J. Forteza, and A. Bohé, *Phys. Rev. D* **93**, 044006 (2016).
- [54] S. Khan, S. Husa, M. Hannam, F. Ohme, M. Pürrer, X. J. Forteza, and A. Bohé, *Phys. Rev. D* **93**, 044007 (2016).
- [55] M. C. Miller, *Astrophys. J.* **581**, 438 (2002).
- [56] J. R. Gair, I. Mandel, M. C. Miller, and M. Volonteri, *Gen. Relativ. Gravit.* **43**, 485 (2011).
- [57] G. D. Quinlan, *New Astron.* **1**, 255 (1996).
- [58] A. Sesana, F. Haardt, P. Madau, and M. Volonteri, *Astrophys. J.* **611**, 623 (2004).
- [59] D. Merritt and M. Milosavljević, *Living Rev. Relativity* **8**, 8 (2005).
- [60] L. S. Finn and K. S. Thorne, *Phys. Rev. D* **62**, 124021 (2000).
- [61] E. A. Huerta, C. J. Moore, P. Kumar, D. George, A. J. K. Chua, R. Haas, E. Wessel, D. Johnson, D. Glennon, A. Rebei, A. M. Holgado, J. R. Gair, and H. P. Pfeiffer, *Phys. Rev. D* **97**, 024031 (2018).
- [62] A. Królak, K. D. Kokkotas, and G. Schäfer, *Phys. Rev. D* **52**, 2089 (1995).
- [63] C. Cutler and J. Harms, *Phys. Rev. D* **73**, 042001 (2006).
- [64] J. Kepler, *Harmonices Mundi* (Linz, 1619).
- [65] L. Wen, *Astrophys. J.* **598**, 419 (2003).